nanomaterials

MDPI

Article

Facile Fabrication of Z-Scheme Bi_2WO_6/WO_3 Composites for Efficient Photodegradation of Bisphenol A with Peroxymonosulfate Activation

Yongkui Huang, Shuangwu Kou, Xiaoting Zhang, Lei Wang, Peili Lu and Daijun Zhang *

State Key Laboratory of Coal Mine Disaster Dynamics and Control, College of Environment and Ecology, Chongqing University, Chongqing 400044, China; huangyk2118@cqu.edu.cn (Y.H.); kousw@cqu.edu.cn (S.K.); xtzhang@cqu.edu.cn (X.Z.); wanglei137319@cqu.edu.cn (L.W.); lupl@cqu.edu.cn (P.L.)

* Correspondence: dzhang@cqu.edu.cn; Tel.: +86-023-6510-5875

Received: 22 March 2020; Accepted: 8 April 2020; Published: 11 April 2020

Abstract: The rational fabrication of direct Z-scheme heterostructures photocatalysts is a pivotal strategy to boost the interfacial charge migration and separation. Herein, direct Z-scheme Bi_2WO_6/WO_3 composites were rationally fabricated for the degradation of bisphenol A combined with the activation of peroxymonosulfate (PMS). The tight interface contact between Bi_2WO_6 and WO_3 was successfully formed by the in situ epitaxial growth of ultrathin Bi_2WO_6 nanosheets at the surface of WO_3 nanorods. The Bi_2WO_6/WO_3 composite presented highly efficient catalytic performance toward degradation of BPA with PMS activation as compared to the WO_3 and Bi_2WO_6. PMS can dramatically boost the photocatalytic activity of the composites. Moreover, the results of active radical scavenging experiments revealed that h^+, $\bullet O_2^-$, and $\bullet SO_4^-$ are critical active species in the photodegradation reaction. Finally, the photocatalytic mechanism for the degradation of BPA is also discussed in detail. The great improvement of photocatalytic performance should be ascribed to the effective formation of the direct Z-scheme heterojunctions between Bi_2WO_6 and WO_3, resulting in improved light absorption, an efficient transfer and separation of photoinduced charge carriers, and a considerable amount of the electrons and holes with strong reduction and oxidation abilities. The study might provide new inspirations to design and construct heterostructured nanomaterials with outstanding photoactivity for environmental remediation.

Keywords: bisphenol A; peroxymonosulfate; photocatalysis; composites; Z-scheme

1. Introduction

Bisphenol A (BPA), as one of a well-known endocrine disrupting compounds (EDCs), has become an environmental concern [1–3]. BPA can be lethal to humans or cause reproductive impairment, diabetes, neurological disorders, cardiovascular disease, and carcinogenic sensitivity [1,3]. BPA is usually used as the raw material for the preparation of epoxy resins, plastics, food containers, water pipes, toys, coatings, medical equipment, and electronics [4,5]. The United States (US) Environmental Protection Agency (EPA) reports that a lot of BPA has entered to the aquatic environment, resulting the ubiquitous presence of BPA in underwater and surface water [2,3]. Thus, it is notably urgent to seek effective techniques to remove BPA from water bodies [1].

Peroxymonosulfate (PMS)-based advanced oxidation processes (AOPs) have aroused considerable attention in environmental remediation [5,6]. PMS could be activated to generate sulfate radicals ($\bullet SO_4^-$) and hydroxyl radicals ($\bullet OH$) [7,8]. The $\bullet SO_4^-$ has been found to be a superior alternative for the environmental remediation of organic contaminants, due to its great advantage, including stronger oxidizing properties, higher oxidation selectivity, and more rapid degradation rate, in contrast to

$\bullet O_2^-$ and •OH [2,6]. PMS can be activated by multifarious methods, such as ultraviolet radiation [8], transition metal ions [9], carbon based materials [10,11], and transition metal composites [2,5]. Unfortunately, most of them are limited by the problems of an external energy input, low activation efficiency, and metal ions leaching [12]. Recently, semiconductor-based photocatalysis is manifested to be a promising strategy for PMS activation to avoid the above potential problems [8,13,14]. More importantly, the coupling of PMS activation and semiconductor-based photocatalysis can not only rapidly and effectively activate PMS toward the formation of $\bullet SO_4^-$, but it can also efficiently accelerate the transfer and separation of photogenerated charges of photocatalysts, leading to an enhanced the catalytic performance [7,13,15]. However, the application of current photocatalytic materials in PMS activation is far from satisfactory due to its insufficient light absorption, low efficiency of photogenerated charge separation, and limited surface active sites [8,16]. Therefore, it is urgently desirable to fabricate novel photocatalytic materials that are highly active and stable for PMS activation.

Tungsten oxide (WO_3) has been considered to be a promising photocatalyst because of its unique optical properties, low cost, chemical stability, and high photoactivity [17,18]. Unfortunately, the photoinduced electrons on the conduction band (CB) of WO_3 cannot efficiently reduce dissolved oxygen to produce $\bullet O_2^-$ radical due to its relatively low CB potential [17,19]. In addition, the photocatalytic applications of WO_3 are also limited due to its inefficient light response, poor conductivity, and serious electron-hole recombination [20–22]. Substantial strategies have been utilized to improve its photocatalytic performances, like doping, deposition of noble metal, introducing surface oxygen vacancy, constructing rational heterostructure, etc. [17,20,23]. In particular, constructing rational heterostructure with other components, such as $BiVO_4$ [21,24], g-C_3N_4 [22,25], and Bi_2WO_6 [9,26], has been reported to greatly improve the photocatalytic performances. In this regard, Bi_2WO_6, a classic of Aurivillius oxide, is an ideal selection for constructing heterojunction composites with WO_3, due to its unique layered structures with composition of the layers of corner-shared WO_6 octahedra sandwiched between the $[Bi_2O_2]^{2+}$ layers [27,28]. However, a weak interactions between each component and complexity of the synthetic protocols seriously block their widespread application potential [28,29]. More unfortunately, the traditional heterojunction photocatalysts will lead to a lower reducibility and oxidizability for photogenerated electrons and holes, which are of great significance in enhancing the catalytic efficiency [22,30–32]. Hence, exploring the in situ formation of direct Z-scheme heterostructures would be a pivotal strategy for addressing the aforementioned problems, which not only attain the strengths of each component, but also introduce some new properties [29,33]. Nevertheless, to the best of our knowledge, the construction of the direct Z-scheme Bi_2WO_6/WO_3 composite with specific structures combined with PMS activated for efficient removal of BPA has never been discovered until now.

In this work, direct Z-scheme Bi_2WO_6/WO_3 composites were firstly fabricated by in situ epitaxial growth method. The Bi^{3+} ions can partially replace the water molecules at the surface of WO_3 nanorods, resulting in a tight interface contact between ultrathin Bi_2WO_6 nanosheets and WO_3 nanorods, which is critically important in constructing efficient heterojunctions. The catalytic activity of the composites were systematically assessed by the photodegradation of BPA combined with the activation of PMS. The Bi_2WO_6/WO_3 composite presented highly efficient catalytic performance toward the degradation of BPA with PMS activation as compared to the WO_3 and Bi_2WO_6. PMS can dramatically boost the photocatalytic activity of the composites. The possible catalytic mechanism for photodegradation of BPA was also investigated in detail. This excellent performance should be ascribed to the effective construction of the direct Z-scheme heterojunctions between Bi_2WO_6 and WO_3, which facilitates the absorption capacity of visible light, promotes the efficient of charge carriers transfer and separation, and provides a considerable amount of the electrons and holes presenting strong reduction and oxidation abilities.

2. Materials and Experimental

2.1. Materials

Bismuth(III) nitrate pentahydrate ($Bi(NO_3)_3{\cdot}5H_2O$), p-benzoquinone (BZQ), BPA, and sodium tungstate dihydrate ($Na_2WO_4{\cdot}2H_2O$) were purchased from Aladdin, Shanghai, China. Hydrochloric acid (HCl), tert-butyl alcohol ($C_4H_{10}O$), potassium persulfate ($K_2S_2O_8$), anhydrous ethanol, methanol, and nitric acid (HNO_3) were purchased from Sinopharm Reagent Co., Shanghai, China.

2.2. Synthesis of Bi_2WO_6/WO_3 Composites

The WO_3 nanorods was fabricated via the procedure reported in previous work [34]. The Bi_2WO_6/WO_3 composites were synthesized by in situ epitaxial growth method. Typically, a certain amount of $Bi(NO_3)_3{\cdot}5H_2O$ was dissolved in 60 mL deionized water. 0.4 g of as-prepared WO_3 nanorods were added in the above solution under vigorous stirring, and then sonicated for 30 min. to ensure WO_3 nanorods disperse well. After another stirring for 30 min., the obtained solution were transferred to a 100 mL Teflon-lined autoclave, then, heated at 160 °C for 16 h. The product was separated by centrifugation, washed by anhydrous ethanol and deionized water several times, and then dried at 60 °C. The various hybrid products were obtained by changing the stoichiometric ratios (Bi:W = 0.8, 1.2, 1.4, and 1.6), which were signed as BW1, BW2, BW3, and BW4, respectively. For comparison, pure Bi_2WO_6 was also fabricated according to the reference [35,36].

2.3. Sample Characterization

The structure of the samples was characterized by the X-ray powder diffraction (XRD, PANalytical X'Pert, Osaka, Japan), Fourier transformation infrared spectra (FT-IR, Nicolet iS50 spectrometer, Thermo Fisher Scientific, Waltham, MA, USA), and Raman spectra (LabRAM HR spectroscopy, HORIBA Jobin Yvon, Longjumeau, France). The morphologies of the samples were collected with Scanning electron microscopy (JSM-7800F electron microscope, Tokyo, Japan) and field emission transmission electron microscope (TEM, Talos F200S electron microscope, Thermo Fisher Scientific, Waltham, MA, USA). The elemental mappings of the samples were carried out with an energy dispersive X-ray spectrometry (EDX, Thermo Fisher Scientific, Waltham, MA, USA). The lattice spacing were obtained by the Digital Micrograph™ software. X-ray photoelectron spectroscopy (XPS) measurement was carried out on a Thermo Fisher Escalab 250Xi X-ray photoelectron spectrometer (Thermo Fisher Scientific, Waltham, MA, USA) with Al $K\alpha$ radiation as the excitation source. The spectra of various elements were calibrated according to C 1s peak (284.8 eV), and fitted by Thermo Avantage v5.952 software with a Shirley background subtraction method. The UV-vis diffuse reflectance spectroscopy spectra (DRS, Shimadzu UV-3600 spectrophotometer with an integrating sphere attachment, Kyoto, Japan) was used to measure the optical properties. The electrochemical measurements were conducted using a standard three-electrode electrochemical system (CHI 660E electrochemical analyzer, Shanghai, China).

2.4. Photocatalytic Performance Tests

The photocatalytic performances of samples were implemented at about 25 °C under visible irradiation. A 300 W Xe arc lamp equipped with a glass filte ($\lambda > 400$ nm) (CELHXF300, China Au-light Co., Ltd., Beijing, China) was employed as the visible light source. The catalysts (50 mg) were dispersed into BPA solution (10 mg/L, 50 mL) with magnetic stirring for 30 min. in order to reach the adsorption and desorption equilibrium. After that, the reaction was initialized by adding PMS under visible light irradiation. 1 mL of aqueous sample was extracted at different intervals and 0.2 mL of methanol was rapidly added to quench the radicals. Unless otherwise specified, the solution pH was 6.9 (natural) and the amounts of PMS was 0.1 mmol/L. The BPA concentration at different time was analyzed on a liquid chromatography (HPLC, Agilent 1260) with a Agilent C-18 column and UV detection wavelength at 276 nm. The mixture solution of 30% water and 70% methanol were used as mobile phase, and the flow rate was 1.0 mL/min.

3. Results and Discussion

3.1. Characterization of Catalysts

The crystalline structures of the prepared photocatalysts have been investigated by XRD. As shown in Figure 1, pure WO_3 represents the main diffraction peaks at 2θ values of 14.1°, 22.9°, 24.4°, 27.0°, 28.3°, 36.6°, 49.2°, 50.1°, and 55.6°, which are in good agreement with the corresponding (100), (001), (110), (101), (200), (201), (301), (220), and (221) planes of hexagonal WO_3 (JCPDS 35-1001) [23,37], respectively. For the Bi_2WO_6/WO_3 composite, the new diffraction peaks at 28.3°, 32.9°, 47.1°, 55.8°, 58.5°, 76.1°, and 78.5° can be corresponded to the (131), (002), (202), (331), (262), (333), and (204) planes of orthorhombic Bi_2WO_6 (JCPDS 39-025), respectively [28,38]. Moreover, the signal of these peaks becomes stronger with a gradual increase of the content of Bi^{3+}, which confirms the formation of Bi_2WO_6. In addition, no additional new phases could be observed, confirming that the high purity of the prepared samples. Notably, the Bi_2WO_6 are successfully grown at the surface of WO_3 nanorods.

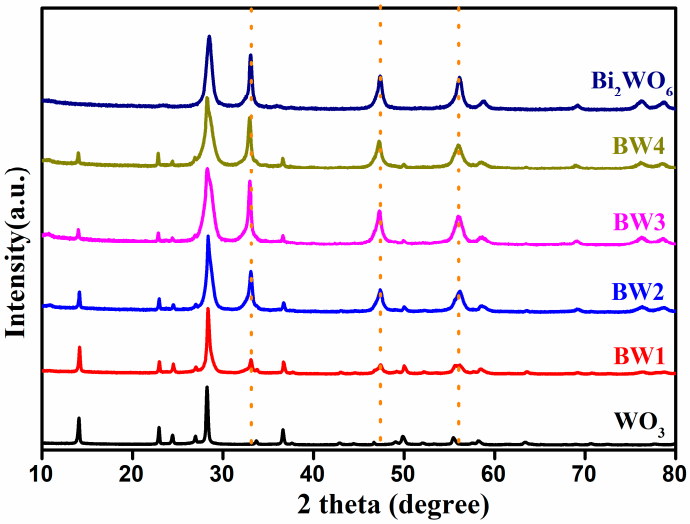

Figure 1. X-ray powder diffraction (XRD) patterns of pure WO_3, Bi_2WO_6, and Bi_2WO_6/WO_3 samples.

The functional groups composition of Bi_2WO_6/WO_3 samples were further studied by FT-IR. As shown in Figure 2, pure WO_3 displays a broad peak at 500–900 cm^{-1}, ascribable to the O–W–O stretching vibration [4,25]. The characteristic peaks of 1600 cm^{-1} is attributed to the bending vibrations of the surface hydroxyl groups, which indicates the presence of the absorbed water molecules on the surface of the sample. As for pure Bi_2WO_6, the peaks located at 548 and 684 cm^{-1} could be assigned to the bridging stretching modes of Bi–O, and the bands of about 820 cm^{-1} belong to the sharing stretching modes of W–O–W [39]. As for the Bi_2WO_6/WO_3 samples, the typical peaks of WO_3 and Bi_2WO_6 are found in the as-prepared Bi_2WO_6/WO_3 composite. With compositional proportion of Bi in the composites increasing, the peak intensities of the Bi_2WO_6 increase, while those of the WO_3 lower gradually. Moreover, the characteristic peaks of Bi_2WO_6 have a clear peak shift, manifesting the good integration in Bi_2WO_6/WO_3 composite is well constructed [4,28]. These results further prove the successful combination of WO_3 nanorods and Bi_2WO_6 in the composites.

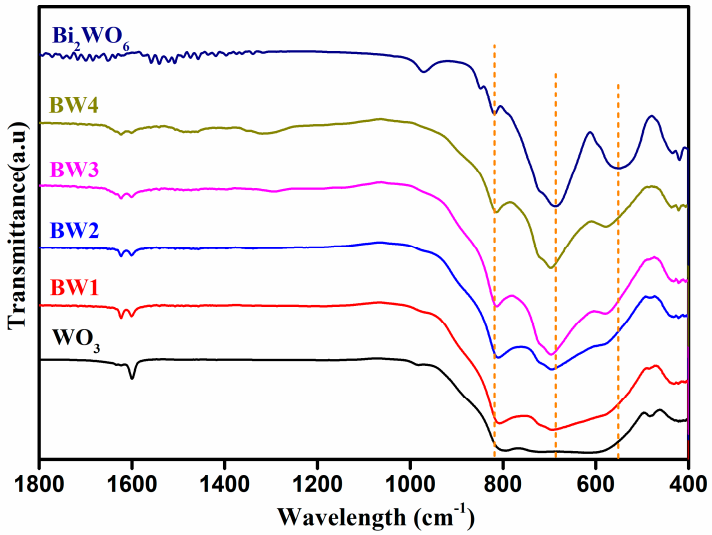

Figure 2. Fourier transformation infrared spectra (FT-IR) spectra of pure WO_3, Bi_2WO_6, and Bi_2WO_6/WO_3 samples.

Raman spectroscopy is used to characterize the bonding states and the local structure of composites. In the Raman spectrum of the pure WO_3 (Figure 3), the band located at 245 and 328 cm^{-1} can be assigned to the O–W–O bending vibration mode, while those band located at 756 and 815 cm^{-1} are ascribed to the W–O stretching vibration mode [4]. For the pure Bi_2WO_6, the band at 309 cm^{-1} is ascribed to the translational modes of Bi^{3+} and $WO_6{}^{6-}$, the band at 417 cm^{-1} is associated with the WO_6 bending (Eu) modes, the band at 700 and 725 cm^{-1} reflect the asymmetric stretching vibration of W–O bond, and the bands at 793 and 820 cm^{-1} are assigned to the terminal O–W–O antisymmetric and symmetric Ag modes [27,28,40]. Bi_2WO_6 and WO_3 are both detected in the composites. These characteristic peaks at 245 and 328 cm^{-1} gradually decreased with the content of Bi_2WO_6 increased, which demonstrates that the contact between WO_3 and Bi_2WO_6 affect the O–W–O bending vibration mode of WO_3 [28,40]. These results further signify the tight contact between Bi_2WO_6 and WO_3 in the Bi_2WO_6/WO_3 composites.

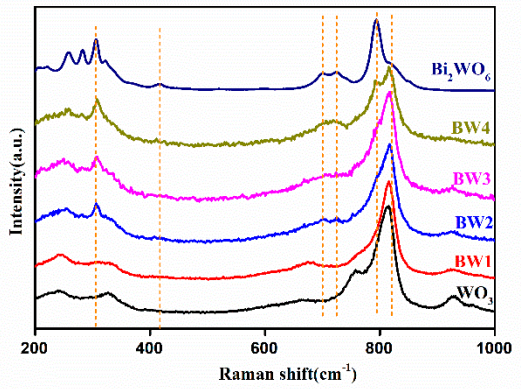

Figure 3. Raman spectra of pure WO_3, Bi_2WO_6, and Bi_2WO_6/WO_3 samples.

SEM was employed to investigate the microstructure of the obtained samples. As presented in Figure 4a,b, the synthesized WO_3 displayed the rodlike morphology, with the diameter from 50 to 200 nm and length from 1 to 3 μm. Figure 4c–e illustrate that the nanocomposites has a multi-slice structure, in which the WO_3 NRs are completely enveloped by the ultrathin Bi_2WO_6 nanosheets. These nanosheets are grown at the surface of WO_3 nanorods and are oriented to different angles. The high-resolution SEM (Figure 4f) indicate these nanosheets have a rough surface and uniform thickness of approximately 8 nm and the length ranged from 200 nm to 2 μm, which could bring more

coordinatively nonsaturable surface-active sites for catalytic reaction. The above results prove that an intimate contact between the Bi_2WO_6 nanosheets and WO_3 nanorods can be readily fabricated by the in situ epitaxial growth method.

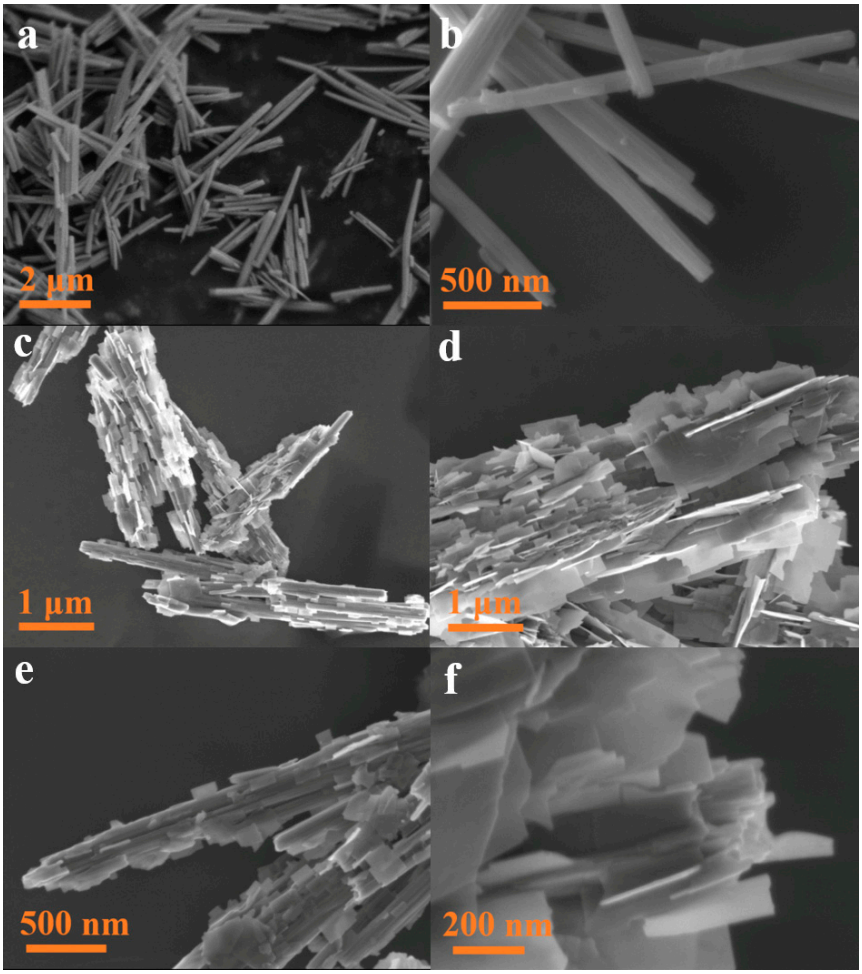

Figure 4. The SEM images of WO_3 (**a**,**b**) and BW3 (**c**–**f**).

The microstructure of the samples were further analyzed by TEM and HRTEM, and the results are presented in Figure 5. WO_3 shows the rod shaped structure with the diameter from 50 to 200 nm, length from 1 to 3 μm. As shown in Figure 5c, the interplanar distance of 0.315 nm is clearly observed, which corresponds to the (200) plane of hexagonal WO_3. Figure 5d,e reveals the BW3 sample was assembled by the ultrathin nanosheets, which are grown from the surface of WO_3 nanorods, and oriented to different angles. The single nanosheet is very thin and estimated to be less than 10 nm. The HRTEM image (Figure 5f) of BW3 sample reveals that these nanosheets exhibit highly crystalline. Furthermore, the lattice distance of 0.273 nm can be clearly identified which corresponds to (200) planes of Bi_2WO_6 [40,41]. In addition, EDS mappings (Figure 5g) reveal that the Bi, W, and O elements are homogeneously distributed over the entire sample. These observations confirm the effective formation of heterojunctions between Bi_2WO_6 and WO_3, which is beneficial for the improvement of photocatalytic efficiency [30,33]. These results are in good agreement with the results of the XRD, Raman, and SEM.

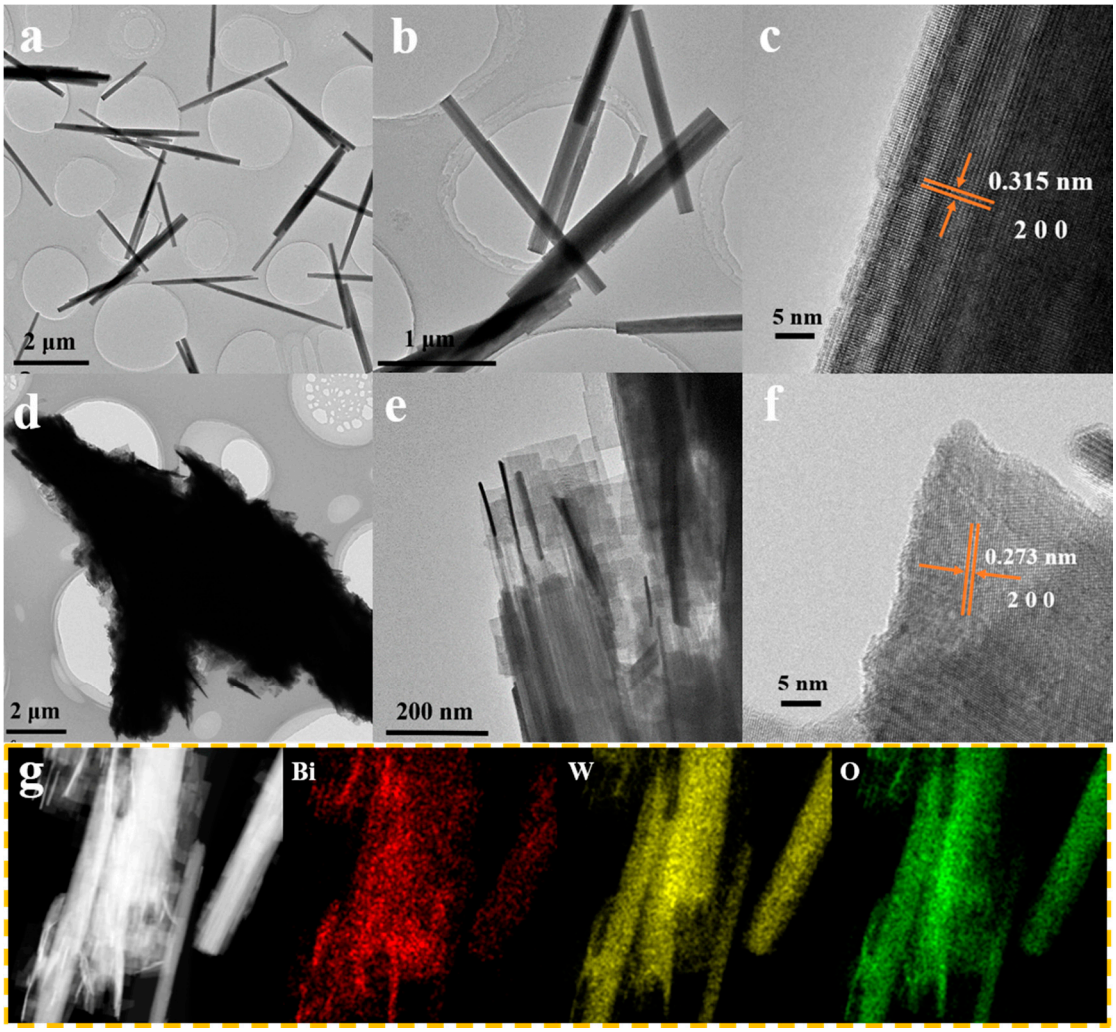

Figure 5. The transmission electron microscope (TEM) and high-resolution-TEM (HRTEM) image of WO_3 (**a**–**c**) and BW3 (**d**–**f**) and the STEM mapping (**g**) of BW3.

The surface chemical states of WO_3 and BW3 were detected by XPS [42]. The survey spectra of WO_3 and BW3 composite are presented in Figure 6a. It can be observed that the WO_3 contains W and O elements, while the BW3 composite contain Bi, W, and O elements, validating Bi_2WO_6 exist in the BW3 composite. The high-resolution spectrum of W 4f (Figure 6b) exhibits two peaks at binding energy of 35.51 and 37.64 eV, which are assigned to W $4f_{7/2}$ and W $4f_{5/2}$ of W^{6+} in WO_3 [19,22]. The characteristic peak of the W 4f in the BW3 composite have slightly shifted to 37.58 and 35.38 eV, which can be assigned to W $4f_{5/2}$ and $4f_{7/2}$, respectively, which indicated that W^{6+} presents in BW3 [43]. From the high-resolution spectrum of Bi 4f (Figure 6c), two characteristic peaks at 164.39 and 159.08 eV are observed in the spectra of BW3, which can be assigned to Bi $4f_{5/2}$ and Bi $4f_{7/2}$ from Bi^{3+} in Bi_2WO_6, respectively [28,43]. For pure WO_3, the O 1s XPS spectra (Figure 6d) centered at 529.6 eV is deconvoluted to characteristic peaks at 530.22 and 532.05 eV, assigned to oxygen group from lattice oxygen and adsorbed oxygen species, respectively [20,30,34]. Nevertheless, the O 1s spectrum of BW3 could be deconvoluted to three peaks at 529.90, 530.49, and 531.63 eV, which are derived from lattice oxygen of $[Bi_2O_2]^{2+}$ and $[WO_4]^{2-}$ and the adsorbed hydrated species, respectively [15,40]. The results demonstrate that the surfaces of WO_3 nanorods are well covered by Bi_2WO_6. These findings further demonstrate that the Bi_2WO_6 are successfully in situ grown at the surface of WO_3 nanorods.

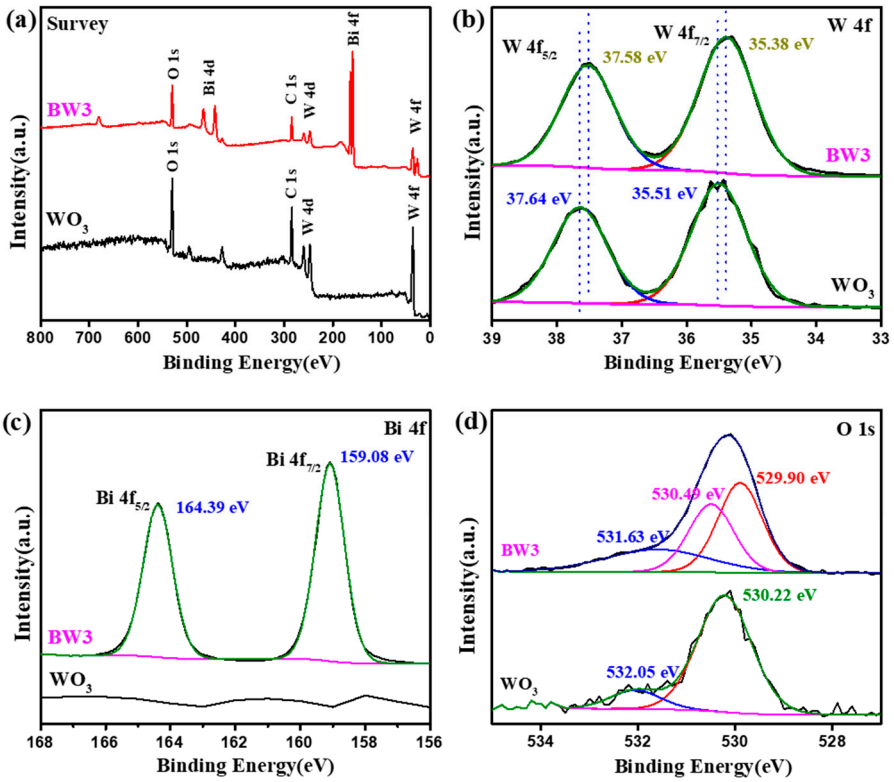

Figure 6. The X-ray photoelectron spectroscopy (XPS) spectra of WO_3 and BW3. (**a**) survey spectra, (**b**) W4f, (**c**) Bi4f, and (**d**) O1s.

The photoabsorption properties of the prepared samples were studied by UV-vis diffuse reflectance spectra (DRS). As shown in Figure 7a, the WO_3 exhibits a absorption edge appeared near 470 nm due to its intrinsic bandgap [20,30]. The pure Bi_2WO_6 displays a absorbance edge at ca. 450 nm because of the charge transfer response of Bi_2WO_6 [36,44]. Obviously, the light absorption intensity of the composites gradually improved with increasing Bi_2WO_6 loadings. It is noted that the absorption edge of the composite has a slight red shift, while the absorption ability of the composite samples increased remarkably. Moreover, the band gap of the samples are acquired according to Kubelka-Munk method (Figure 7b). The band gap of WO_3, Bi_2WO_6, BW1, BW2, BW3, and BW4 are estimated to be 2.74, 2.81, 2.80, 2.78, 2.77, and 2.75 eV, respectively. This result unambiguously confirms the formation of Bi_2WO_6/WO_3 heterojunction structure. Therefore, it is reasonable to infer that the composite samples could harness more visible light, and form more electron-hole pairs, signifying the superior photocatalytic activity.

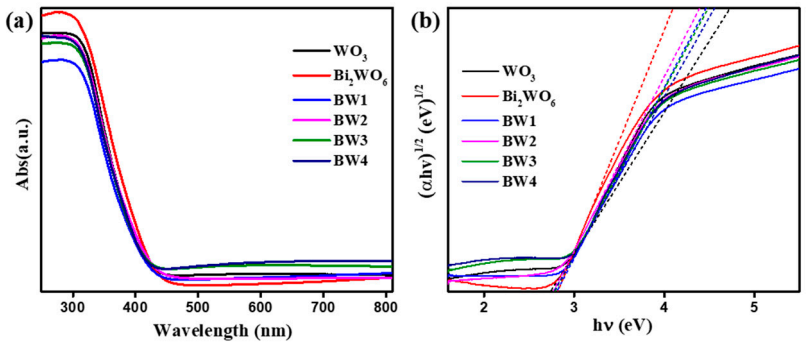

Figure 7. UV-vis diffused reflection spectra (**a**) and Tauc's plots (**b**) of pure WO_3, Bi_2WO_6, and Bi_2WO_6/WO_3 samples.

3.2. Photocatalytic Performance

The photodegradation of BPA in the presence of PMS was employed as the probe reaction to evaluate the photocatalytic efficiency of the prepared materials. As depicted in Figure 8, the prepared materials have different adsorption capacity. It can be seen that 9.5%, 9.4%, and 3.9% of BPA were adsorbed by WO_3, Bi_2WO_6, and BW3 within 30 min., respectively. Obviously, the prepared materials show only small amounts of BPA adsorption abilities. Under visible-light irradiation, the remove efficiency is very low in the absence of photocatalysts, indicating that single PMS could hardly degrade BPA [7,13,14]. Moreover, WO_3 and Bi_2WO_6 exhibit weak photocatalytic performance with PMS activation, and only 18.1 and 32.0% of BPA are removed within 30 min., respectively. Clearly, the BW3 exhibits remarkable photocatalytic efficiency as compared to the WO_3 and Bi_2WO_6. Only 43.0% of BPA can be degraded by BW3 after 20 min. of visible light irradiation, while removal efficiency can be achieved to 94.7% with PMS activation. These results unambiguously proves that the introduction of PMS effectively improves the photocatalytic efficiency of the composites. Therefore, it is concluded that the heterojunction is formed between the interfaces of Bi_2WO_6 and WO_3, thus leading to promoting the photocatalytic activity in PMS activation and photodegradation of BPA.

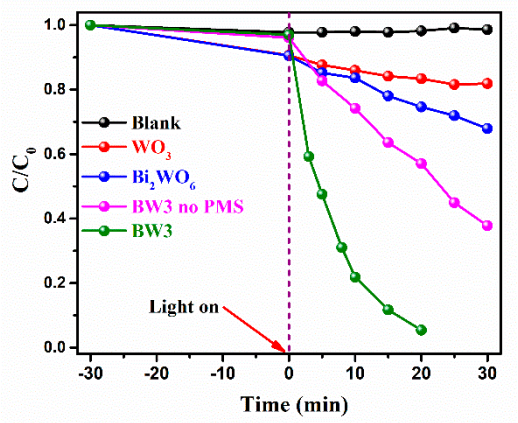

Figure 8. The degradation efficiency of Bisphenol A (BPA) under visible light irradiation over various samples. Reaction condition: initial BPA concentration of 10 mg/L, peroxymonosulfate (PMS) dosage of 0.1 mmol/L, catalyst addition of 1 g/L.

The influence of stoichiometric ratios of Bi and W in the composites for the BPA degradation was further evaluated. As illustrated in Figure 9a, the stoichiometric ratios of Bi and W has a significant influence on photodegradation of BPA with PMS activation. As the stoichiometric ratios of Bi and W increased from 0.8 to 1.4, the photocatalytic activities of the composites improve gradually and the BW3 shows the highest photocatalytic activity. It is mainly attributed to the effective formation of heterojunctions between two components, which could enhance the visible light absorption and improve the separation efficiency of charge carriers in the composites. However, the catalytic efficiency decreased with further increasing the stoichiometric ratios of Bi:W to 1.6. It is concluded that excessive Bi_2WO_6 at the surface of the WO_3 would dramatically decrease active sites on the heterojunctions. Furthermore, the photocatalytic degradation kinetics of BPA can be further evaluated by fitting the experimental data to following pseudo first-order kinetics Equation (Figure 9b). The apparent rate constant (k) is estimated to be 0.008, 0.015, 0.016, 0.045, 0.145, and 0.143 for WO_3, Bi_2WO_6, BW1, BW2, BW3, and BW4, respectively. The BW3 sample exhibits the highest photodegradation rate of BPA with PMS activation, which is approximately 18.1 and 9.6 times higher than that of WO_3 and Bi_2WO_6. Therefore, suitable stoichiometric ratios of Bi:W in the composites are necessary for optimizing the catalytic activity for BPA photodegradation with PMS activation.

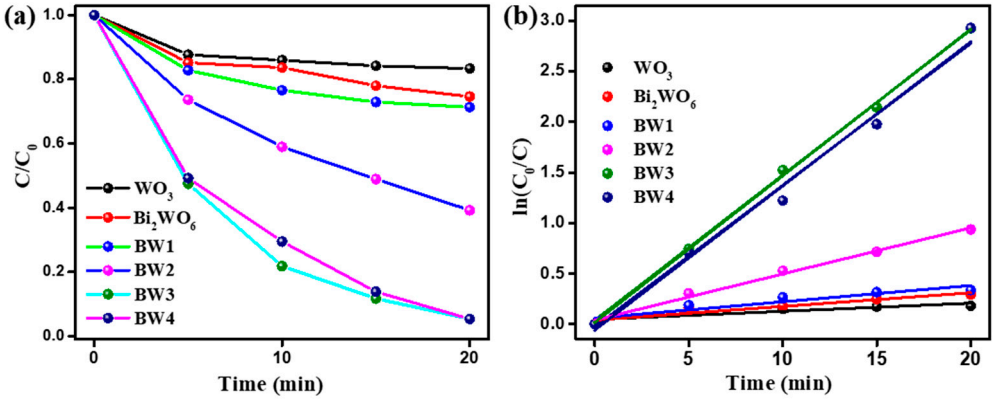

Figure 9. The influence of stoichiometric ratios of Bi and W in the composites for the BPA degradation (**a**), and the corresponding degradation kinetics of BPA (**b**). Reaction condition: initial BPA concentration of 10 mg/L, PMS dosage of 0.1 mmol/L, catalyst addition of 1 g/L.

3.3. Photodegradation Mechanism of the Samples

The active radicals that were involved in the photocatalytic degradation of BPA under the BW3 with PMS activation were investigated by the radical trapping experiments. In these process, isopropanol (IPA, 10 mmol/L), ethylenediaminetetraacetic acid disodium salt (EDTA, 10 mmol/L), methanol (MeOH, 10 mmol/L), and benzoquinone (BZQ, 0.1 mmol/L) were severed as the scavengers for hydroxyl radical (•OH), holes (h^+), and sulfate radical ($\bullet SO_4^-$) and superoxide radical ($\bullet O_2^-$), respectively [7,13]. Figure 10 shows that the photocatalytic activity slightly decreased in the presence of IPA, which implied that the •OH has a little role in photodegradation reaction. Moreover, the introducing BZQ, EDTA, and MeOH in the reactive solutions can lead to a significant inhibition for BPA degradation. Overall, the inhibition for BPA degradation ranked in the sequence of EDTA > BZQ > MeOH > IPA. The above results exhibit that h^+, $\bullet O_2^-$, and $\bullet SO_4^-$ are major active species for BPA degradation over BW3, while the •OH plays a minor role in reaction process.

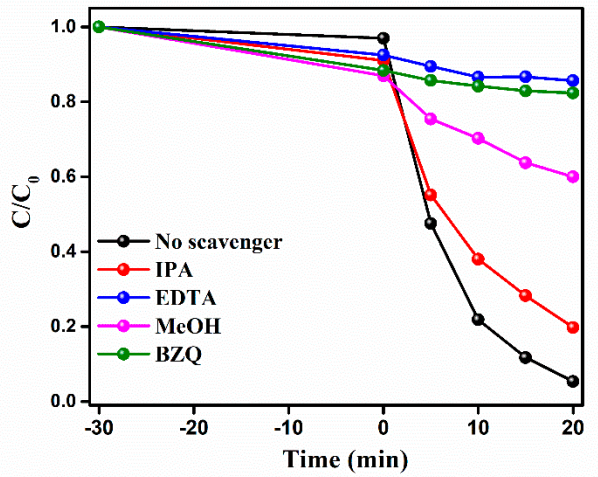

Figure 10. The photocatalytic degradation of BPA over BW3 with PMS activation in the presence of different scavengers. Reaction condition: initial BPA concentration of 10 mg/L, PMS dosage of 0.1 mmol/L, catalyst addition of 1 g/L.

The electrochemical impedance spectra (EIS) and photocurrent responses were conducted to explore the interfacial charge separation efficiency, and the results are depicted in Figure 11. Generally, a lower radius of the Nyquist plot represents a faster interfacial charge transport [45,46]. As shown in Figure 11a, the arc radius of EIS Nyquist circle of BW3 is smaller than those of single WO_3 and

Bi_2WO_6. The results reveal that BW3 exhibits highly efficient separation and transfer of photoinduced charge carriers. Moreover, the photocurrent density of 0.7, 1.4 and 3.3 μAcm^{-2} can be obtained for WO_3, Bi_2WO_6 and BW3 under identical conditions, respectively (Figure 11b). Obviously, BW3 has superior photocurrent response. Therefore, it can be inferred that the photoinduced charge carriers in the Bi_2WO_6/WO_3 composites can fleetly transfer between the WO_3 and Bi_2WO_6, and the formed heterojunction interface effectively inhibited the direct recombination of electron-hole pairs.

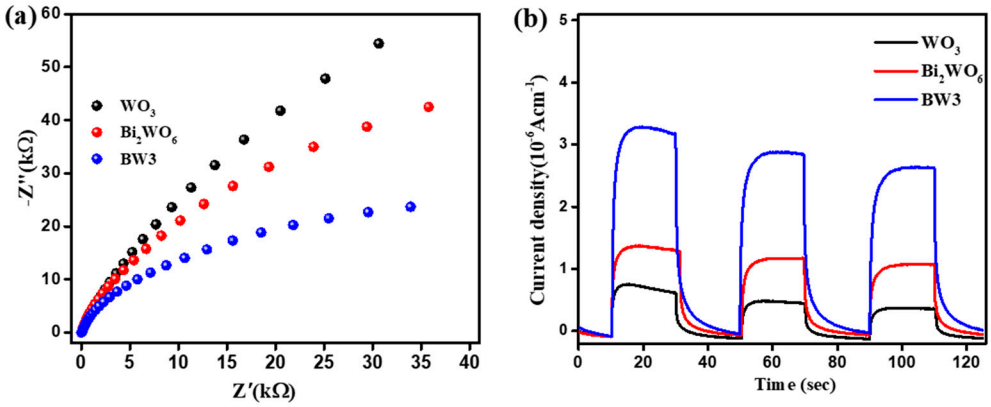

Figure 11. Electrochemical impedance spectra (EIS) (**a**) and photocurrents responses (**b**) of WO_3, Bi_2WO_6 and BW3 composite.

Based on these analyses, the possible catalytic mechanism for BPA photodegradation over the Bi_2WO_6/WO_3 composites with PMS activation can be schematically illustrated in Figure 12. The WO_3 and Bi_2WO_6 could generate the photogenerated holes and electrons under visible light irradiation, because their band gaps are about 2.64 and 2.81 eV, respectively [22,39]. In addition, the CB and VB edge position of Bi_2WO_6 is −1.04 and 1.77 eV (vs NHE), and the CB and VB edge position of WO_3 is 0.77 and 3.41 eV (vs NHE), respectively [22,47,48]. Therefore, two kinds of transfer and separation of carrier transfer might be possible, according to the band arrangement principle. The first type is the type-II heterojunction architectures (Figure 12a). When irradiated by visible light, WO_3 and Bi_2WO_6 are both excited to generate electrons-holes pairs. Subsequently, the generated electrons of CB in Bi_2WO_6 can inject into the CB of WO_3, and the holes could cross from the VB of WO_3 to the VB of BW. Hence, the electrons are accumulated in the CB of WO_3, and the holes are accumulated in the VB of Bi_2WO_6. However, the photogenerated electrons could not efficiently react with dissolved oxygen to generate $\bullet O_2^-$ radicals, because the position of CB of WO_3 is lower than the standard potential of $O_2/\bullet O_2^-$ (−0.33 eV vs. NHE) [22,37]. Meanwhile, the holes on the VB of Bi_2WO_6 are too weak to generate •OH [39,47]. Therefore, a heterojunction-type electron transfer is not appropriate in the present system, which is inconsistent with the results of the trapping radical experiment.

Therefore, the Z-scheme mechanism would properly explain the photocatalytic process and is shown in Figure 12b. In this case, the photogenerated electrons are transferred from the CB of WO_3 to the VB of Bi_2WO_6, and recombined with the photogenerated holes that are generated on the VB of Bi_2WO_6, resulting in abundant photoexcited electrons on the CB of the Bi_2WO_6, and holes on the VB of WO_3. Consequently, these photogenerated charge carriers have supreme oxidation and reduction abilities to stimulate the photocatalytic process. The electrons accumulated in the CB of the Bi_2WO_6 can react with dissolved oxygen to generate $\bullet O_2^-$ radicals. Simultaneously, the electrons could be efficiently captured by PMS to generate $\bullet SO_4^-$, which can not only provide highly reactive oxygen species for BPA photodegradation, but also greatly accelerate the separation of charge carriers [13,14]. The photoexcited holes that accumulated on the VB of WO_3 can directly oxidize BPA into the nontoxic products. The •OH are produced by the oxidize reaction of the holes with surface-adsorbed water or OH^- on the surfaces of BW. Besides, •OH can also be generated by the conversion of $\bullet O_2^-$ or PMS [7,13]. Consequently, the $\bullet SO_4^-$, $\bullet O_2^-$, h^+, and •OH can efficiently decompose BPA in the photocatalytic

process. Therefore, it can be concluded that the effective formation of Z-scheme heterojunctions between Bi_2WO_6 and WO_3 facilitates the absorption capacity of visible-light, promotes the efficient transfer and separation of charge carriers, and provides more supreme oxidation and reduction abilities of electrons and holes.

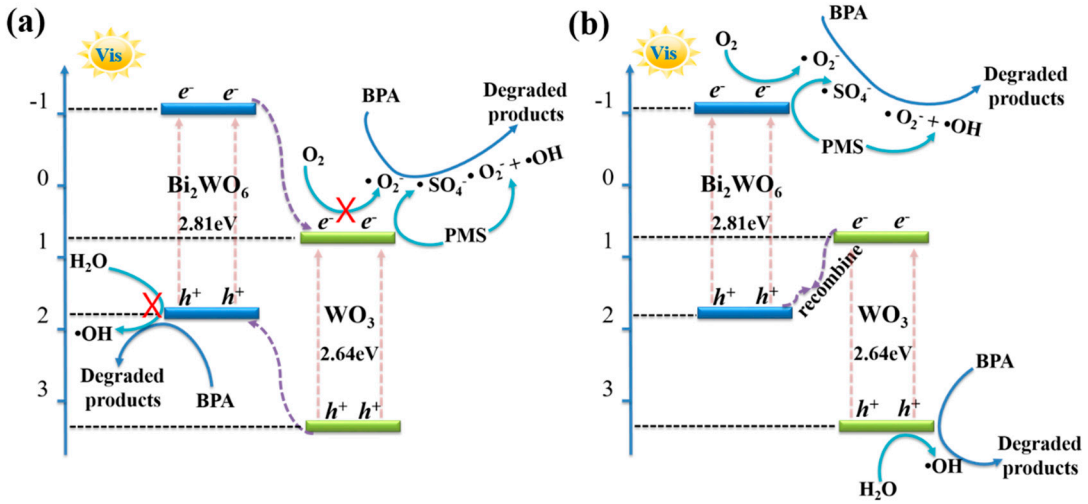

Figure 12. The proposed catalytic mechanisms of Bi_2WO_6/WO_3 composite: (**a**) the type-II heterojunction; (**b**) the Z-scheme.

4. Conclusions

In summary, direct Z-scheme Bi_2WO_6/WO_3 composite was rationally fabricated in order to degrade BPA with the activation of PMS under visible light irradiation. The tight interface contact between Bi_2WO_6 and WO_3 is successfully realized by in situ epitaxial growth of ultrathin Bi_2WO_6 nanosheets at the surface of WO_3 nanorods. The Bi_2WO_6/WO_3 composites exhibited remarkably enhanced photocatalytic activity toward the degradation of BPA with PMS activation as compared to the WO_3 and Bi_2WO_6. PMS could dramatically boost the photocatalytic activity of the composites. In addition, the stoichiometric ratios of Bi:W has significant influence on the photocatalytic activity of the composites. Moreover, the results of trapping radical experiment reveals that h^+, $\bullet O_2^-$, and $\bullet SO_4^-$ are critical active species in the photocatalytic reaction. Finally, the possible catalytic mechanism for BPA degradation was also discussed in detail. Such an excellent performance should be attributed to the effective formation of direct Z-scheme heterojunctions between Bi_2WO_6 and WO_3, which facilitates the capacity of light absorption, promotes the efficient transfer and separation of photoinduced charge carriers, and provides more supreme oxidation and reduction abilities of the electrons and holes. The study might provide new inspirations to design and construct heterostructured nanomaterials with outstanding photoactivity for environmental remediation.

Author Contributions: Conceptualization, Y.H. and D.Z.; Investigation, Y.H., S.K. and X.Z.; Writing, Original Draft Preparation, Y.H.; Writing, Review and Editing, L.W., P.L. and D.Z.; Supervision, D.Z.; Funding Acquisition, D.Z. All authors have read and agreed to the published version of the manuscript.

Funding: This research was funded by the Natural Science Foundation of China (51808067 and 51778083), the Chongqing Special Postdoctoral Science Foundation (XmT2018054), the China Postdoctoral Science Foundation (2017M622969), and the Scientific Research Foundation of State Key Laboratory of Coal Mine Disaster Dynamics and Control (2011DA105287-ZD201505, 2011DA105287-MS201806).

Acknowledgments: The authors would express our gratitude to analytical and testing center of Chongqing University for the instrumental support.

Conflicts of Interest: The authors declare no conflict of interest.

References

1. Chen, D.; Kannan, K.; Tan, H.; Zheng, Z.; Feng, Y.L.; Wu, Y.; Widelka, M. Bisphenol analogues other than bpa: Environmental occurrence, human exposure, and toxicity-a review. *Environ. Sci. Technol.* **2016**, *50*, 5438–5453. [CrossRef] [PubMed]
2. Huang, G.X.; Wang, C.Y.; Yang, C.W.; Guo, P.C.; Yu, H.Q. Degradation of bisphenol A by peroxymonosulfate catalytically activated with $Mn_{1.8}Fe_{1.2}O_4$ nanospheres: Synergism between Mn and Fe. *Environ. Sci. Technol.* **2017**, *51*, 12611–12618. [CrossRef] [PubMed]
3. Lee, G.J.; Lee, X.Y.; Lyu, C.; Liu, N.; Andandan, S.; Wu, J.J. Sonochemical synthesis of copper-doped $BiVO_4$/g-C_3N_4 nanocomposite materials for photocatalytic degradation of bisphenol A under simulated sunlight irradiation. *Nanomaterials* **2020**, *10*, 498. [CrossRef] [PubMed]
4. Fu, J.; Xu, Q.; Low, J.; Jiang, C.; Yu, J. Ultrathin 2D/2D WO_3/g-C_3N_4 step-scheme H_2-production photocatalyst. *Appl. Catal. B Environ.* **2019**, *243*, 556–565. [CrossRef]
5. Wang, F.; Lai, Y.; Fang, Q.; Li, Z.; Ou, P.; Wu, P.; Duan, Y.; Chen, Z.; Li, S.; Zhang, Y. Facile fabricate of novel Co(OH)F@MXenes catalysts and their catalytic activity on bisphenol A by peroxymonosulfate activation: The reaction kinetics and mechanism. *Appl. Catal. B Environ.* **2020**, *262*. [CrossRef]
6. Li, X.; Huang, X.; Xi, S.; Miao, S.; Ding, J.; Cai, W.; Liu, S.; Yang, X.; Yang, H.; Gao, J.; et al. Single cobalt atoms anchored on porous N-doped graphene with dual reaction sites for efficient fenton-like catalysis. *J. Am. Chem. Soc.* **2018**, *140*, 12469–12475. [CrossRef] [PubMed]
7. Zhang, H.; Nengzi, L.C.; Wang, Z.; Zhang, X.; Li, B.; Cheng, X. Construction of Bi_2O_3/CuNiFe LDHs composite and its enhanced photocatalytic degradation of lomefloxacin with persulfate under simulated sunlight. *J. Hazard. Mater.* **2020**, *383*, 121236. [CrossRef]
8. Hao, X.; Wang, G.; Chen, S.; Yu, H.; Quan, X. Enhanced activation of peroxymonosulfate by CNT-TiO_2 under UV-light assistance for efficient degradation of organic pollutants. *Front. Environ. Sci. Eng.* **2019**, *13*. [CrossRef]
9. Rong, F.; Wang, Q.; Lu, Q.; Yao, L.; Wei, M. Rational fabrication of hierarchical Z-Scheme WO_3/Bi_2WO_6 nanotubes for superior photoelectrocatalytic reaction. *ChemistrySelect* **2019**, *4*, 2676–2684. [CrossRef]
10. Gao, Y.; Chen, Z.; Zhu, Y.; Li, T.; Hu, C. New insights into the generation of singlet oxygen in the metal-free peroxymonosulfate activation process: Important role of electron-deficient carbon atoms. *Environ. Sci. Technol.* **2020**, *54*, 1232–1241. [CrossRef]
11. Huang, B.C.; Huang, G.X.; Jiang, J.; Liu, W.J.; Yu, H.Q. Carbon-Based catalyst synthesized and immobilized under calcium salt assistance to boost singlet oxygen evolution for pollutant degradation. *ACS Appl. Mater. Interfaces* **2019**, *11*, 43180–43187. [CrossRef] [PubMed]
12. Lim, J.; Yang, Y.; Hoffmann, M.R. Activation of peroxymonosulfate by oxygen vacancies-enriched cobalt-doped black TiO_2 nanotubes for the removal of organic pollutants. *Environ. Sci. Technol.* **2019**, *53*, 6972–6980. [CrossRef] [PubMed]
13. Zeng, Y.; Guo, N.; Xu, X.; Yu, Y.; Wang, Q.; Wang, N.; Han, X.; Yu, H. Degradation of bisphenol a using peroxymonosulfate activated by WO_3@MoS_2/Ag hollow nanotubes photocatalyst. *Chemosphere* **2019**, *227*, 589–597. [CrossRef] [PubMed]
14. Li, R.; Huang, J.; Cai, M.; Huang, J.; Xie, Z.; Zhang, Q.; Liu, Y.; Liu, H.; Lv, W.; Liu, G. Activation of peroxymonosulfate by Fe doped g-C_3N_4 /graphene under visible light irradiation for Trimethoprim degradation. *J. Hazard. Mater.* **2020**, *384*, 121435. [CrossRef]
15. Sayed, M.; Khan, J.A.; Shah, L.A.; Shah, N.S.; Shah, F.; Khan, H.M.; Zhang, P.; Arandiyan, H. solar light responsive poly(vinyl alcohol)-assisted hydrothermal synthesis of immobilized TiO_2/Ti film with the addition of peroxymonosulfate for photocatalytic degradation of ciprofloxacin in aqueous media: A mechanistic approach. *J. Phys. Chem. C* **2017**, *122*, 406–421. [CrossRef]
16. Tan, X.; Bai, J.; Zheng, J.; Zhang, Y.; Li, J.; Zhou, T.; Xia, L.; Xu, Q.; Zhou, B. Photocatalytic fuel cell based on sulfate radicals converted from sulfates in situ for wastewater treatment and chemical energy utilization. *Catal. Today* **2019**, *335*, 485–491. [CrossRef]
17. Tahir, M.B.; Ali, S.; Rizwan, M. A review on remediation of harmful dyes through visible light-driven WO_3 photocatalytic nanomaterials. *Int. J. Environ. Sci. Technol.* **2019**, *16*, 4975–4988. [CrossRef]

18. Yang, M.Q.; Gao, M.; Hong, M.; Ho, G.W. Visible-to-NIR photon harvesting: Progressive engineering of catalysts for solar-powered environmental purification and fuel production. *Adv. Mater.* **2018**, *30*, e1802894. [CrossRef]
19. Xiao, T.; Tang, Z.; Yang, Y.; Tang, L.; Zhou, Y.; Zou, Z. In situ construction of hierarchical WO_3/g-C_3N_4 composite hollow microspheres as a Z-scheme photocatalyst for the degradation of antibiotics. *Appl. Catal. B Environ.* **2018**, *220*, 417–428. [CrossRef]
20. Li, S.; Hu, S.; Jiang, W.; Zhang, J.; Xu, K.; Wang, Z. In situ construction of WO_3 nanoparticles decorated Bi_2MoO_6 microspheres for boosting photocatalytic degradation of refractory pollutants. *J. Colloid Interface Sci.* **2019**, *556*, 335–344. [CrossRef]
21. Du, H.; Pu, W.; Wang, Y.; Yan, K.; Feng, J.; Zhang, J.; Yang, C.; Gong, J. Synthesis of $BiVO_4$/WO_3 composite film for highly efficient visible light induced photoelectrocatalytic oxidation of norfloxacin. *J. Alloys Compd.* **2019**, *787*, 284–294. [CrossRef]
22. Singh, J.; Arora, A.; Basu, S. Synthesis of coral like WO_3/g-C_3N_4 nanocomposites for the removal of hazardous dyes under visible light. *J. Alloys Compd.* **2019**, *808*. [CrossRef]
23. Tang, S.; Courte, M.; Peng, J.; Fichou, D. Oxygen-deficient WO_3 via high-temperature two-step annealing for enhanced and highly stable water splitting. *Chem. Commun.* **2019**, *55*, 7958–7961. [CrossRef] [PubMed]
24. Kumbhar, V.S.; Lee, H.; Lee, J.; Lee, K. Interfacial growth of the optimal $BiVO_4$ nanoparticles onto self-assembled WO_3 nanoplates for efficient photoelectrochemical water splitting. *J. Colloid Interface Sci.* **2019**, *557*, 478–487. [CrossRef]
25. Han, X.; Xu, D.; An, L.; Hou, C.; Li, Y.; Zhang, Q.; Wang, H. WO_3/g-C_3N_4 two-dimensional composites for visible-light driven photocatalytic hydrogen production. *Int. J. Hydrogen Energy* **2018**, *43*, 4845–4855. [CrossRef]
26. Gui, M.-S.; Zhang, W.-D.; Chang, Y.-Q.; Yu, Y.-X. One-step hydrothermal preparation strategy for nanostructured WO_3/Bi_2WO_6 heterojunction with high visible light photocatalytic activity. *Chem. Eng. J.* **2012**, *197*, 283–288. [CrossRef]
27. Cao, X.; Chen, Z.; Lin, R.; Cheong, W.-C.; Liu, S.; Zhang, J.; Peng, Q.; Chen, C.; Han, T.; Tong, X.; et al. A photochromic composite with enhanced carrier separation for the photocatalytic activation of benzylic C–H bonds in toluene. *Nat. Catal.* **2018**, *1*, 704–710. [CrossRef]
28. Xing, Z.; Hu, J.; Ma, M.; Lin, H.; An, Y.; Liu, Z.; Zhang, Y.; Li, J.; Yang, S. From one to two: In situ construction of an ultrathin 2D-2D closely bonded heterojunction from a single-phase monolayer nanosheet. *J. Am. Chem. Soc.* **2019**, *141*, 19715–19727. [CrossRef]
29. Meng, S.; Ning, X.; Zhang, T.; Chen, S.F.; Fu, X. What is the transfer mechanism of photogenerated carriers for the nanocomposite photocatalyst Ag_3PO_4/g-C_3N_4, band-band transfer or a direct Z-scheme? *Phys. Chem. Chem. Phys. PCCP* **2015**, *17*, 11577–11585. [CrossRef]
30. Chai, B.; Liu, C.; Yan, J.; Ren, Z.; Wang, Z.-j. In-situ synthesis of WO_3 nanoplates anchored on g-C_3N_4 Z-scheme photocatalysts for significantly enhanced photocatalytic activity. *Appl. Surf. Sci.* **2018**, *448*, 1–8. [CrossRef]
31. Huang, Y.; Zhang, X.; Zhang, K.; Lu, P.; Zhang, D. Facile fabrication of sandwich-like BiOI/AgI/g-C_3N_4 composites for efficient photocatalytic degradation of methyl orange and reduction of Cr(VI). *J. Nanoparticle Res.* **2018**, *20*. [CrossRef]
32. Yadav, H.M.; Kim, J.-S. Solvothermal synthesis of anatase TiO_2-graphene oxide nanocomposites and their photocatalytic performance. *J. Alloys Compd.* **2016**, *688*, 123–129. [CrossRef]
33. Low, J.; Dai, B.; Tong, T.; Jiang, C.; Yu, J. In situ irradiated X-Ray photoelectron spectroscopy investigation on a direct Z-Scheme TiO_2/CdS composite film photocatalyst. *Adv. Mater.* **2019**, *31*, e1802981. [CrossRef] [PubMed]
34. Weng, B.; Wu, J.; Zhang, N.; Xu, Y.J. Observing the role of graphene in boosting the two-electron reduction of oxygen in graphene-WO_3 nanorod photocatalysts. *Langmuir* **2014**, *30*, 5574–5584. [CrossRef]
35. Tang, J.; Zou, Z.; Ye, J. Photocatalytic decomposition of organic contaminants by Bi_2WO_6 under visible light irradiation. *Catal. Lett.* **2004**, *92*, 53–56. [CrossRef]
36. Sun, S.; Wang, W.; Xu, J.; Wang, L.; Zhang, Z. Highly efficient photocatalytic oxidation of phenol over ordered mesoporous Bi_2WO_6. *Appl. Catal. B Environ.* **2011**, *106*, 559–564. [CrossRef]

37. Ke, J.; Zhou, H.; Liu, J.; Zhang, Z.; Duan, X.; Wang, S. Enhanced light-driven water splitting by fast electron transfer in 2D/2D reduced graphene oxide/tungsten trioxide heterojunction with preferential facets. *J. Colloid Interface Sci.* **2019**, *555*, 413–422. [CrossRef]
38. Wang, J.; Tang, L.; Zeng, G.; Deng, Y.; Dong, H.; Liu, Y.; Wang, L.; Peng, B.; Zhang, C.; Chen, F. 0D/2D interface engineering of carbon quantum dots modified Bi_2WO_6 ultrathin nanosheets with enhanced photoactivity for full spectrum light utilization and mechanism insight. *Appl. Catal. B Environ.* **2018**, *222*, 115–123. [CrossRef]
39. Huang, Y.K.; Kang, S.F.; Yang, Y.; Qin, H.F.; Ni, Z.J.; Yang, S.J.; Li, X. Facile synthesis of Bi/Bi_2WO_6 nanocomposite with enhanced photocatalytic activity under visible light. *Appl. Catal. B Environ.* **2016**, *196*, 89–99. [CrossRef]
40. Zhou, H.; Wen, Z.; Liu, J.; Ke, J.; Duan, X.; Wang, S. Z-scheme plasmonic Ag decorated WO_3/Bi_2WO_6 hybrids for enhanced photocatalytic abatement of chlorinated-VOCs under solar light irradiation. *Appl. Catal. B Environ.* **2019**, *242*, 76–84. [CrossRef]
41. Zhang, C.; Chen, G.; Lv, C.; Yao, Y.; Xu, Y.; Jin, X.; Meng, Q. Enabling nitrogen fixation on Bi_2WO_6 photocatalyst by c-PAN surface decoration. *ACS Sustain. Chem. Eng.* **2018**, *6*, 11190–11195. [CrossRef]
42. Santos, V.C.; Wilson, K.; Lee, A.F.; Nakagaki, S. Physicochemical properties of WO_x/ZrO_2 catalysts for palmitic acid esterification. *Appl. Catal. B Environ.* **2015**, *162*, 75–84. [CrossRef]
43. Zhang, M.; Lai, C.; Li, B.; Huang, D.; Liu, S.; Qin, L.; Yi, H.; Fu, Y.; Xu, F.; Li, M.; et al. Ultrathin oxygen-vacancy abundant WO_3 decorated monolayer Bi_2WO_6 nanosheet: A 2D/2D heterojunction for the degradation of Ciprofloxacin under visible and NIR light irradiation. *J. Colloid Interface Sci.* **2019**, *556*, 557–567. [CrossRef] [PubMed]
44. Cao, S.; Shen, B.; Tong, T.; Fu, J.; Yu, J. 2D/2D Heterojunction of ultrathin MXene/Bi_2WO_6 nanosheets for improved photocatalytic CO_2 reduction. *Adv. Funct. Mater.* **2018**, *28*. [CrossRef]
45. Hou, T.; Xiao, Y.; Cui, P.; Huang, Y.; Tan, X.; Zheng, X.; Zou, Y.; Liu, C.; Zhu, W.; Liang, S.; et al. Operando oxygen vacancies for enhanced activity and stability toward nitrogen photofixation. *Adv. Energy Mater.* **2019**, *9*. [CrossRef]
46. Kong, S.; An, Z.; Zhang, W.; An, Z.; Yuan, M.; Chen, D. Preparation of hollow flower-like microspherical beta-Bi_2O_3/BiOCl heterojunction and high photocatalytic property for tetracycline hydrochloride degradation. *Nanomaterials* **2019**, *10*, 57. [CrossRef]
47. Liu, Y.; Wei, B.; Xu, L.; Gao, H.; Zhang, M. Generation of oxygen vacancy and OH radicals: A comparative study of Bi_2WO_6 and Bi_2WO_{6-x} Nanoplates. *ChemCatChem* **2015**, *7*, 4076–4084. [CrossRef]
48. Zhang, Y.; Zhang, N.; Tang, Z.-R.; Xu, Y.-J. Identification of Bi_2WO_6 as a highly selective visible-light photocatalyst toward oxidation of glycerol to dihydroxyacetone in water. *Chem. Sci.* **2013**, *4*, 1820. [CrossRef]